



Facile synthesis and enhanced catalytic performance of reduced graphene oxide decorated with hexagonal structure Ni nanoparticles

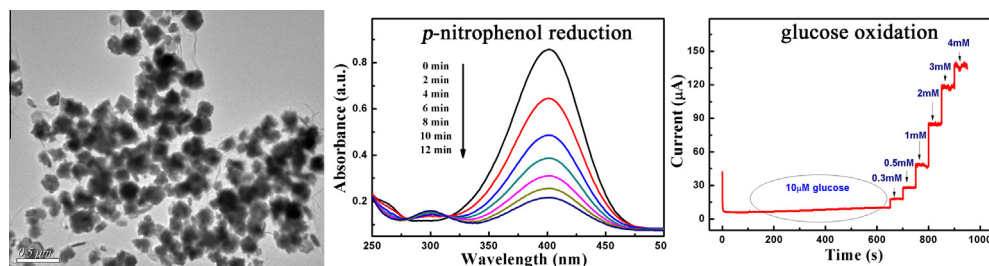


Zhenyuan Ji^a, Yuqin Wang^a, Xiaoping Shen^{a,*}, Hanyu Ma^a, Juan Yang^{a,*}, Aihua Yuan^b, Hu Zhou^b

^a School of Chemistry and Chemical Engineering, School of Environment and Safety Engineering, Jiangsu University, Zhenjiang 212013, PR China

^b School of Environmental and Chemical Engineering, Jiangsu University of Science and Technology, Zhenjiang 212003, PR China

GRAPHICAL ABSTRACT



ARTICLE INFO

Article history:

Received 2 August 2016

Revised 10 October 2016

Accepted 18 October 2016

Available online 19 October 2016

Keywords:

Graphene

Nickel

Nanocomposites

Synthesis

Catalysis

ABSTRACT

In this study, reduced graphene oxide (RGO) supported Ni nanoparticles were synthesized by a facile in-situ refluxing approach using triethylene glycol as both reductive and dispersing agent. The as-synthesized RGO/Ni nanocomposites were characterized by X-ray diffraction, Raman spectroscopy and transmission electron microscopy, which revealed that Ni nanoparticles with hexagonal close-packed structure were homogeneously dispersed on the surface of RGO sheets. The catalytic activity and electrochemical properties of the RGO/Ni nanocomposites were investigated. It is found that the RGO/Ni nanocomposites exhibit markedly enhanced catalytic activity toward the reduction of *p*-nitrophenol by NaBH_4 , which is comparable to noble metal catalyst. The RGO/Ni nanocomposites also exhibited excellent electrocatalytic response to glucose. The linear range, detection limit and sensitivity were estimated to be 0.01–3.0 mM ($R^2 = 0.997$), 2.8 μM and 535.258 $\mu\text{A mM}^{-1} \text{cm}^{-2}$, respectively. It is expected that this facile method presented here could be extended to synthesize other RGO/metal nanocomposites with various functions.

© 2016 Elsevier Inc. All rights reserved.

1. Introduction

In recent years, the research on the catalysis of metal nanoparticles has been developing at an extraordinary pace due to their high density of states near Fermi levels [1,2]. Noble metal nanoparticles are of particular interest in catalysis due to their high chemical stability and catalytic activity [3]. However, high cost

and a finite availability of noble metals strongly limit their practical catalytic applications. Thus, in order to avoid the usage of noble metals, non-precious transition metal catalysts become the first choice in many catalytic processes. Among them, nickel metal has received much attention because of its potential applications in hydrogen storage, electrochemical capacitors, magnetic devices, microwave absorption, as well as catalysis in various chemical reactions [4–8]. Notably, to maximize the catalytic activity of nickel metal, loading the nickel nanoparticles on the suitable supporting materials is highly desirable [9].

* Corresponding author.

E-mail address: xiaopingshen@163.com (X. Shen).

Over the past two decades, carbon nanomaterials as the solid supports to disperse and stabilize the metal nanoparticles in catalytic process have received a great attention by the researchers. Since its discovery in 2004, graphene has initiated an explosive interest as one of the ideal support among all the carbonaceous materials due to its outstanding properties, such as unique sheet structure, extremely large surface area, high mechanical stiffness, as well as superior chemical stability [10–12]. The synergetic effects between graphene and nanomaterials can enhance the catalytic properties and improve the functionalities of the graphene-based nanocomposites [13–16]. Up to now, some investigations have been done on the synthesis of graphene supported nickel nanoparticles for improving the properties of nickel metal. However, despite the significant efforts, there still exist some challenges and problems in the study of graphene/Ni nanocomposites: (i) many of the synthesis approaches to graphene/Ni nanocomposites suffer from the use of hazardous or toxic reducing agents, and their use should be avoided in the large-scale production. (ii) The nickel nanoparticles supported on graphene are mainly face-centered cubic structure, hexagonal close-packed structure Ni is rarely reported. Specifically, Yang and co-workers established a facile chemical approach to grow hexagonal close-packed Ni nanocrystals on graphene, which exhibit excellent microwave absorbability [17]. However, an organic stabilizer (octadecylamine) is required during the procedure, and the catalytic properties of the as-prepared graphene/Ni nanocomposites are not studied yet. Therefore, it is desirable to develop an environmentally friendly and facile approach to prepare hexagonal close-packed nickel supported on graphene with excellent catalytic properties.

Very recently, we have developed an in-situ reduction approach for the synthesis of RGO-supported and wrapped nickel nanoparticles with face-centered cubic structure, which show enhanced catalytic properties [18]. Continuing with this line of research, in the present manuscript we present a facile refluxing approach for the synthesis of RGO supported hexagonal close-packed Ni nanoparticles using triethylene glycol as both reductive and dispersing agent. In addition, the catalytic properties of the RGO/Ni nanocomposites in the reduction of *p*-nitrophenol by NaBH₄ and electrocatalytic oxidation of glucose are systematically investigated.

2. Experimental

2.1. Materials

Natural flake graphite (45 μm, 99.95%) was obtained from Aladdin Industrial Corporation (Shanghai, China). All of the other reagents employed in this study are commercially available analytical-grade and used as received without further purification. Graphite oxide was synthesized by the oxidative treatment of natural flake graphite using a modified Hummers method reported previously [19,20].

2.2. Preparation of RGO/Ni nanocomposites

In a typical procedure to synthesize the RGO/Ni nanocomposites, 25 mg of graphite oxide was dispersed in 50 mL of triethylene glycol by ultrasonication to form a homogeneous dispersion. Subsequently, 0.3 g of nickel acetylacetonate was added to the above system. After stirring for about 15 min, the resulting mixture was then transferred into a 100 mL round-bottomed flask and heated at 270 °C under magnetic stirring for 1 h. The solid products were separated by centrifugation, washed thoroughly with water and ethanol to remove any impurities, and then dried in a vacuum oven at 45 °C for 12 h. RGO/Ni nanocomposites with different Ni loadings were prepared by simply varying the feed amount of

nickel acetylacetonate with other experimental conditions unchanged. The obtained samples were denoted as RGO/Ni-0.2 and RGO/Ni-0.35 for feeding 0.2 and 0.35 g of nickel acetylacetonate, respectively. Pure RGO and Ni were also obtained through a similar procedure in the absence of nickel acetylacetonate and graphite oxide, respectively.

2.3. Instrumentation and measurements

Powder X-ray diffraction (XRD) measurements were carried out on an X-ray diffractometer (Shimadzu XRD-6100 Lab) with Cu Kα radiation ($\lambda = 1.5406 \text{ \AA}$) at a scanning rate of 5° min^{-1} . The morphology and size of the products were examined by transmission electron microscopy (TEM) and high resolution TEM (HRTEM, JEOL JEM-2100). The loading amounts of Ni in the RGO/Ni nanocomposites were evaluated by an inductively coupled plasma-optical emission spectrometer (ICP-OES, Vista-MXP, Varian). Raman scattering was collected at room temperature using a DXR Raman spectrometer with 532 nm laser source from an Ar⁺ laser. The X-ray photoelectron spectroscopy (XPS) measurements were performed by using a Thermo ESCALAB 250XI spectrometer. Ultraviolet-visible (UV-vis) spectroscopy measurements were recorded with a UV-1800PC UV-vis spectrophotometer.

2.4. Catalytic reduction of *p*-nitrophenol

In a typical procedure, the aqueous solutions of *p*-nitrophenol (10 mM) and NaBH₄ (1.0 M) were freshly prepared. Then, 5 mg of catalysts and 2 mL of NaBH₄ solution were added to 100 mL of distilled water under magnetic stirring. After stirring for about 15 min, 0.5 mL of 4-NP solution was then added to start the reaction. The reaction was carried out at room temperature with continuous stirring until the deep yellow color of the solution became colorless. During the reaction process, a small portion of the reaction mixture was quickly withdrawn from the reaction system, followed by measuring UV-vis absorption spectra of the solution to monitor the concentration of *p*-nitrophenol through its absorption peak at 400 nm.

2.5. Electrocatalytic experiments

The electrocatalytic properties of the RGO/Ni nanocomposites toward glucose were carried out on a beaker-type three-electrode setup using a CHI 760D electrochemical analyzer (Chen Hua Instruments, Shanghai, China) at room temperature. Platinum wire, saturated calomel electrode (SCE) and glassy carbon (3 mm in diameter) coated with nanocomposites were used as counter electrode, reference electrode and working electrode, respectively. Before surface modification, the glassy carbon electrode was polished with 1.0, 0.3, and 0.05 μm alumina powders sequentially, followed by sonication in ethanol and distilled water successively. Then the washed glassy carbon electrode was dried at room temperature and ready for modification. To obtain the RGO/Ni nanocomposites modified glassy carbon electrode, 5.0 mg of RGO/Ni powder and 20 μL of Nafion solution (5 wt%, Alfa Aesar) were dispersed in 1.0 mL of ethanol and ultrasonicated for 30 min to form a homogeneous catalyst ink. A total of 6 μL of the RGO/Ni dispersion was dropped on the clean surface of glassy carbon electrode and was allowed to dry in ambient air. Using the modified RGO/Ni working electrode, cyclic voltammetry was conducted in an aqueous solution with an electrolyte of 0.1 M NaOH at room temperature. The cyclic voltammetry measurements required operation of the electrode in a range of potential of 0.1–0.6 V versus SCE. Amperometric measurements were performed by successive injection of a certain concentration of

glucose solution into the stirring 0.1 M NaOH solution, and the current was recorded when it reached the steady state.

3. Results and discussion

3.1. Structural and morphological characterization

Herein, an efficient one-step refluxing approach was developed for the fabrication of RGO/Ni nanocomposites. Typically, nickel acetylacetonate was first mixed with the pre-synthesized GO colloidal suspension. After being heated at 270 °C for 1 h, the Ni²⁺ ions were in-situ reduced to form Ni nanoparticles, while GO nanosheets were reduced to RGO at the same time. Thus, RGO/Ni nanocomposites were successfully prepared. The phase structure of the as-synthesized samples was firstly determined by XRD (Fig. 1a). In the case of graphite oxide, the obvious peak centered at 2θ of about 11° corresponds to the (001) reflection of graphite oxide [21]. For Ni nanoparticles, the characteristic peaks, in good agreement with the standard data of Ni (JCPDS no. 45-1027), can be indexed to hexagonal structured Ni. The peaks originate from (010), (002), (011), (012), (110), and (103) crystal planes, respectively. The RGO/Ni nanocomposites show similar XRD pattern. The major diffraction peaks in RGO/Ni nanocomposites are in accordance with the XRD pattern of Ni. The weak and broad peak at 2θ of about 25° originates from the short-range ordered stacking of graphene nanosheets, which indicates that graphite oxide in RGO/Ni nanocomposites has been well flaked and reduced. Fig. 1b shows the typical Raman spectra of graphite oxide and RGO/Ni nanocomposites. Two prominent characteristic peaks can be observed in both the samples, which are attributed to well-documented in-plane A_{1g} zone-edge mode (D band) and the doubly degenerate zone center E_{2g} mode (G band), respectively [22,23]. The peak integrated intensity ratio of D to G bands (I_D/I_G) provides the gauge for the amount of the defects and the degree of disorder in carbon structure [24,25]. In this case, the I_D/I_G ratios for graphite oxide and RGO/Ni nanocomposites are 1.36 and 1.89, respectively. This result implies that an increase in the number of defects was produced after the introduction of Ni nanoparticles on the RGO sheets.

Important information about the near-surface chemical compositions of graphite oxide and RGO/Ni nanocomposites can be further provided by XPS analysis (Fig. 2). C1s and O1s peaks can be observed in the XPS survey scan of graphite oxide (Fig. 2a). In the XPS spectra of RGO/Ni nanocomposites, the element composition of the composite including C, O and Ni was further identified from the full survey scan XPS spectrum. The peaks located at 854.9 and 872.5 eV in Fig. 2b are assigned to the binding energy of Ni

2p_{3/2} and Ni 2p_{1/2}, which reveals that the zero valent Ni is obtained after reduction from Ni²⁺ [26]. The higher energy bands with relatively low intensities located at 860.6 and 879.2 eV can be attributed to a higher oxidation state of Ni, formed by inevitable oxidation upon the exposure to air. Fig. 2c and d shows the high-resolution C1s spectra of the graphite oxide and RGO/Ni, which can be deconvoluted into four different peaks that correspond to C entities with different oxidation states. The peaks located at the binding energies of 284.7, 286.6, 287.2, and 288.7 eV can be assigned to C–C in aromatic rings, C–O (epoxy and hydroxy), C=O (carbonyl), and O=C–O (carboxyl) groups, respectively [27,28]. With the refluxing process, the intensities of XPS peaks of the carbon atoms bonded to oxygen decreased significantly in the spectrum of RGO/Ni nanocomposites. Further analysis of this XPS spectrum indicates that the C/O molar ratio increases from 1.9 of graphite oxide to 3.2 of RGO/Ni, indicating the effective removal of oxygen-containing functional groups in GO sheets.

In order to clearly observe the size, morphology and micro-structure of the as-prepared samples, TEM measurement was performed. Fig. 3 shows the representative TEM images of the synthesized RGO/Ni nanocomposites and bare Ni. Partially folded and crumpled morphology that is characteristic feature of RGO nanosheets can be observed in Fig. 3a and b, and the surface of RGO sheets is uniformly decorated with Ni nanoparticles. Almost no free Ni nanoparticles are found outside of the RGO sheets throughout the TEM observation process, indicating that the combination between Ni nanoparticles and RGO nanosheets is highly effective. The layers of RGO has been characterized by HRTEM. Fig. S1a presents the HRTEM image of RGO nanosheets in RGO/Ni nanocomposites. The arrow indicates a RGO platelet consisting of 6 graphene layers. HRTEM image of Ni nanoparticles (Fig. S1b) revealed clear lattice fringes with an interplanar distance of 0.203 nm, which could be assigned to the (011) plane of hexagonal Ni. The size of the Ni nanoparticles in the nanocomposites is determined to be about 231 nm (Fig. 3c). The content of Ni in RGO/Ni nanocomposites was about 67 wt% according to ICP-OES analysis. The morphology of bare Ni was also analyzed by TEM to specifically investigate the influence of RGO on the morphology of the Ni clusters. The TEM images in Fig. 3d show a significant aggregation of the Ni nanoparticles. It indicates that RGO may interact with Ni nanoparticles and inhibit their aggregation after incorporation of them into composite materials. Graphene oxide, as is known, can be regarded as an unconventional polymeric species, would play a role as a polymeric surfactant in the reaction system [29,30]. It may work as stabilizer or capping agent to inhibit the aggregation of the Ni nanoparticles and result in a relatively uniform distribution of Ni on RGO sheets.

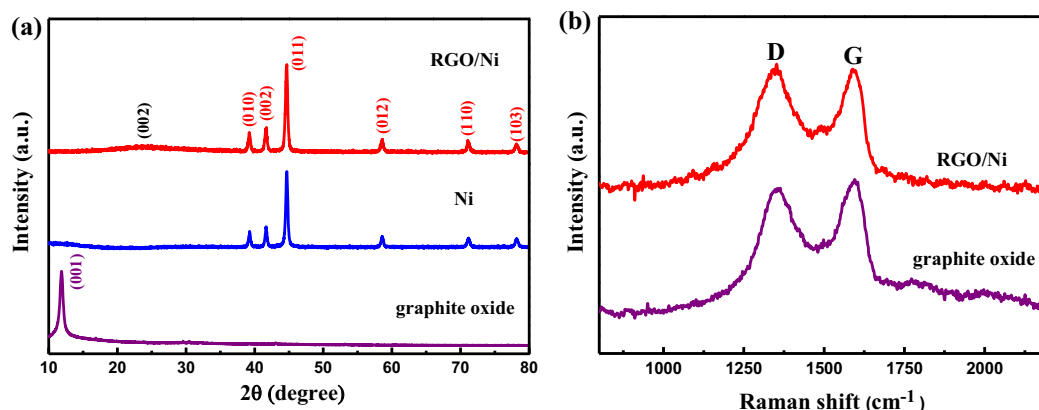


Fig. 1. (a) XRD patterns and (b) Raman spectra of graphite oxide, Ni, RGO/Ni nanocomposites.

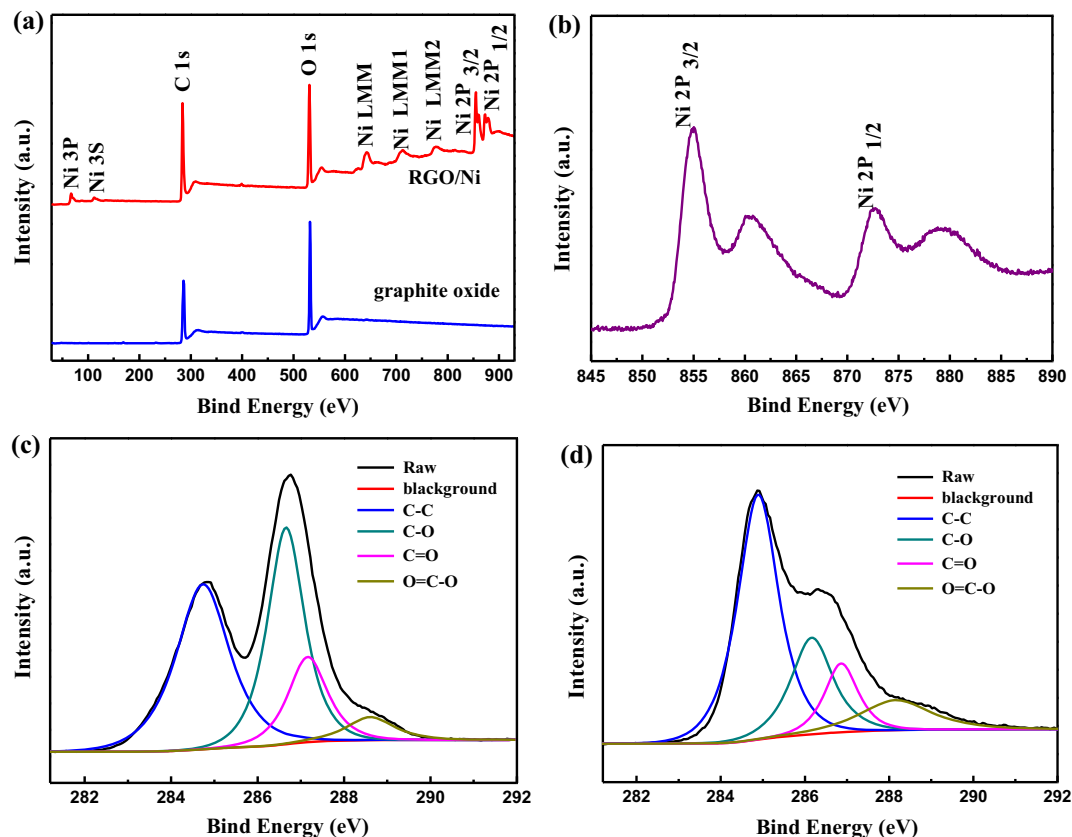


Fig. 2. (a) XPS survey scan of graphite oxide and RGO/Ni nanocomposites; (b) Ni 2p peaks of RGO/Ni nanocomposites; High-resolution C1s spectra of (c) graphite oxide and (d) RGO/Ni nanocomposites.

3.2. Catalytic properties toward *p*-nitrophenol

As is known, *p*-nitrophenol is a common organic pollutant that can occur in agricultural and industrial waste water. In this study, the catalytic performance of the RGO/Ni nanocomposites was firstly quantitatively evaluated with the reduction of *p*-nitrophenol by NaBH₄ as a model reaction. This reaction is kinetically restricted in the absence of a catalyst. After the addition of a small amount of RGO/Ni nanocomposites into the above reaction system, the yellow solution gradually became colorless, indicating that the catalytic reaction occurred. The catalytic process of this reaction was also monitored by time-dependent UV–vis absorption spectra. As can be seen from Fig. 4a, the absorption peak at 400 nm gradually weakens because of the decreasing concentration of *p*-nitrophenol, while a new peak centered at 300 nm appears due to the formation of *p*-aminophenol as the reaction time increases.

It is proposed that the reaction follows the pseudo-first-order kinetics with respect to the concentration of *p*-nitrophenol when excess NaBH₄ was used [31]. In the reaction system, the ratio of C_t and C₀, where C_t and C₀ are *p*-nitrophenol concentrations at time *t* and 0, respectively, was measured from the ratio of the absorbances (A_t/A₀) at 400 nm. Good linear correlations of ln(A_t/A₀) versus time *t* are observed, confirming the pseudo-first-order kinetics (Fig. 4b). From the slopes of the straight lines, the apparent rate constants for different catalysts can be obtained. The rate constant of RGO/Ni nanocomposites is about 0.126 min⁻¹, which is about three times higher than that of bare Ni catalyst (0.047 min⁻¹). In addition, it is found that the content of Ni in the nanocomposites has an important effect on the catalytic efficiency. From Fig. S2, it can be seen that with the increase of Ni content in RGO/Ni nanocomposites, the catalytic activity increased at first and then decreased. The RGO/Ni nanocomposites

prepared with 0.3 g nickel acetylacetonate exhibits the best catalytic activity toward the *p*-nitrophenol reduction. The catalytic activity of RGO/Ni was even higher than that of commercial Raney Ni catalyst, indicating the excellent catalytic performance of the RGO/Ni nanocomposites. The rate constant is also comparable to that of noble metal catalysts in the reduction of *p*-nitrophenol, but the RGO/Ni composite is much cheaper [31]. In this study, we also evaluated the catalytic stability of the RGO/Ni nanocomposites by monitoring catalytic activity during successive cycles of the reduction reaction. As shown in Fig. S3, the catalytic efficiency only displays a slight decrease without significant loss of activity after five cycles. In addition, the interplanar distance of Ni nanoparticles (Fig. S4) does not display noticeable changes after catalysis, which confirms the high stability of the catalysts. Since bare RGO do not show obvious catalytic activity (Fig. 4b), it is deduced that the catalytic activity of RGO/Ni nanocomposites originates from Ni, while RGO serve as synergist. The possible reaction mechanism for *p*-nitrophenol reduction by NaBH₄ can be proposed in terms of the Langmuir-Hinshelwood model as follows [32]: BH₄⁻ will adsorb on the surface of the Ni nanoparticles and transfer a surface-hydrogen species to the surface of Ni nanoparticles. Concomitantly, the nitrophenolate ions will then adsorb onto the Ni surface via nitro group, and then receive electrons generated from the reaction of BH₄⁻ and proton to form aminophenols. When the product of *p*-aminophenol desorbs leaving free Ni surface, the catalytic cycle can begin again. The RGO sheets with higher adsorption ability toward *p*-nitrophenol via π-π stacking interaction would provide a drive for enriching *p*-nitrophenol molecules to the Ni nanoparticle catalyst [33,34]. On the other hand, as evidenced by the TEM images, RGO can offer an environment to inhibit the aggregation of bare Ni nanoparticles and obstruct the loss of catalytic activity.

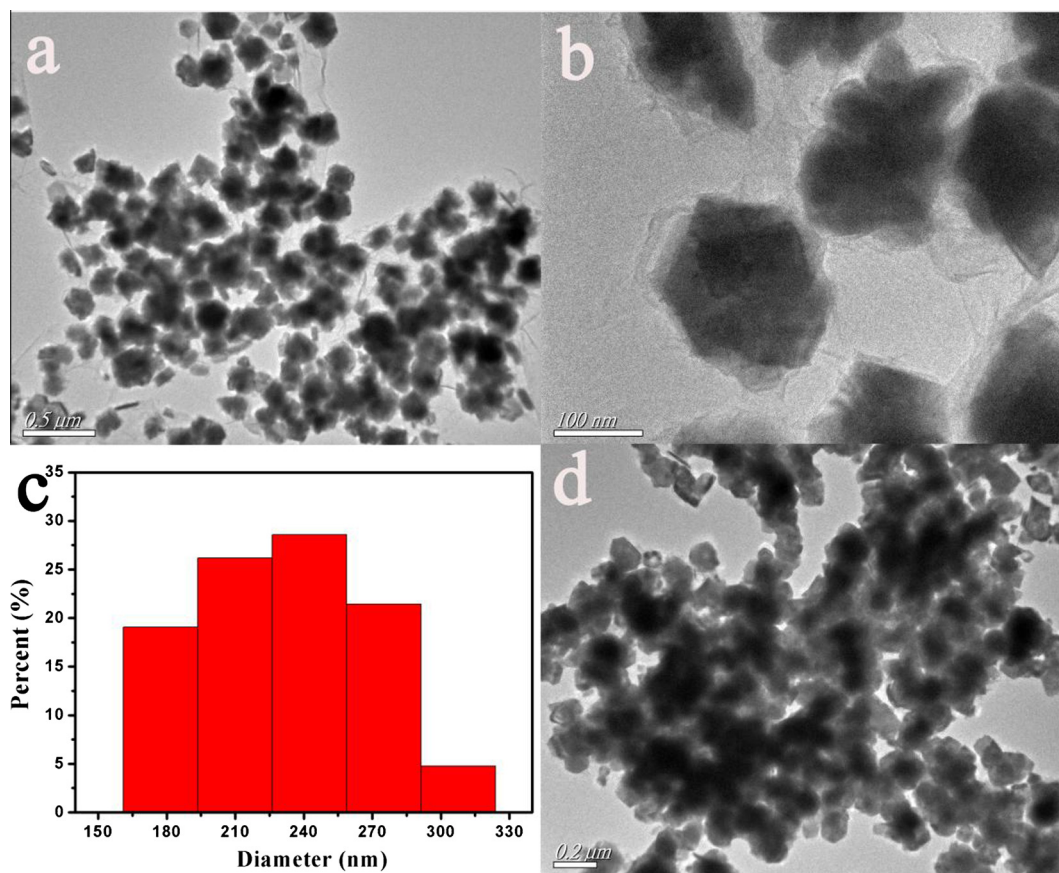


Fig. 3. (a and b) TEM images of RGO/Ni nanocomposites; (c) The size distribution of Ni nanoparticles in the nanocomposites; (d) TEM image of bare Ni.

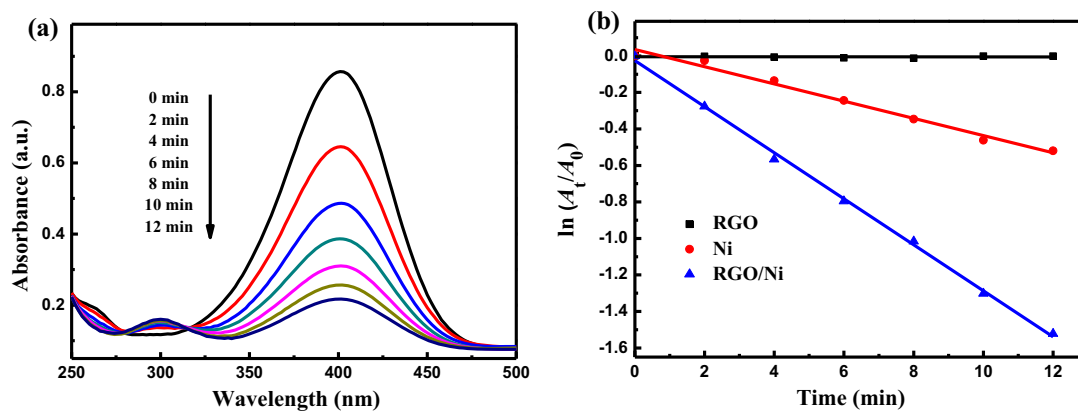


Fig. 4. Successive UV-vis spectra for the reduction of *p*-nitrophenol by NaBH_4 with RGO/Ni as catalyst; (b) Pseudo first order plots of $\ln(A_t/A_0)$ of *p*-nitrophenol versus reaction time over different catalysts.

3.3. Catalytic properties toward glucose

It is well known that diabetes mellitus is a worldwide public health problem and thus the detection of glucose is particularly important [35]. Based on the enhanced catalytic activity of RGO/Ni nanocomposites toward the reduction of *p*-nitrophenol, the electrocatalytic oxidation of glucose in an alkaline medium was also investigated in this work. Cyclic voltammetry was carried out in a three electrode system over a potential range from 0.1 to 0.6 V with 0.1 M NaOH solution as the electrolyte. Fig. 5a presents the representative cyclic voltammograms for RGO/Ni nanocomposites electrode under different scan rates (10–100 mV/s). It is found

that all of the cyclic voltammograms show a pair of redox peaks, which are assigned to the Ni(II)/Ni(III) redox couple in the alkaline medium [36,37]. In addition, the cyclic voltammograms become wider with the increasing scan rates from 10 to 100 mV/s, and the potentials of the oxidation peak and reduction peak shift to the positive and the negative directions, respectively. From Fig. 5b, it can be seen that both anodic and cathodic peak currents are linearly proportional to the square root of scan rate with high correlation coefficient of 0.998 and 0.993. This reveals that the electrode reaction in RGO/Ni is dominated by a diffusion controlled kinetics with a fast electron transfer rate during the electrocatalytic process [38]. Fig. 5c shows the electrocatalytic responses of

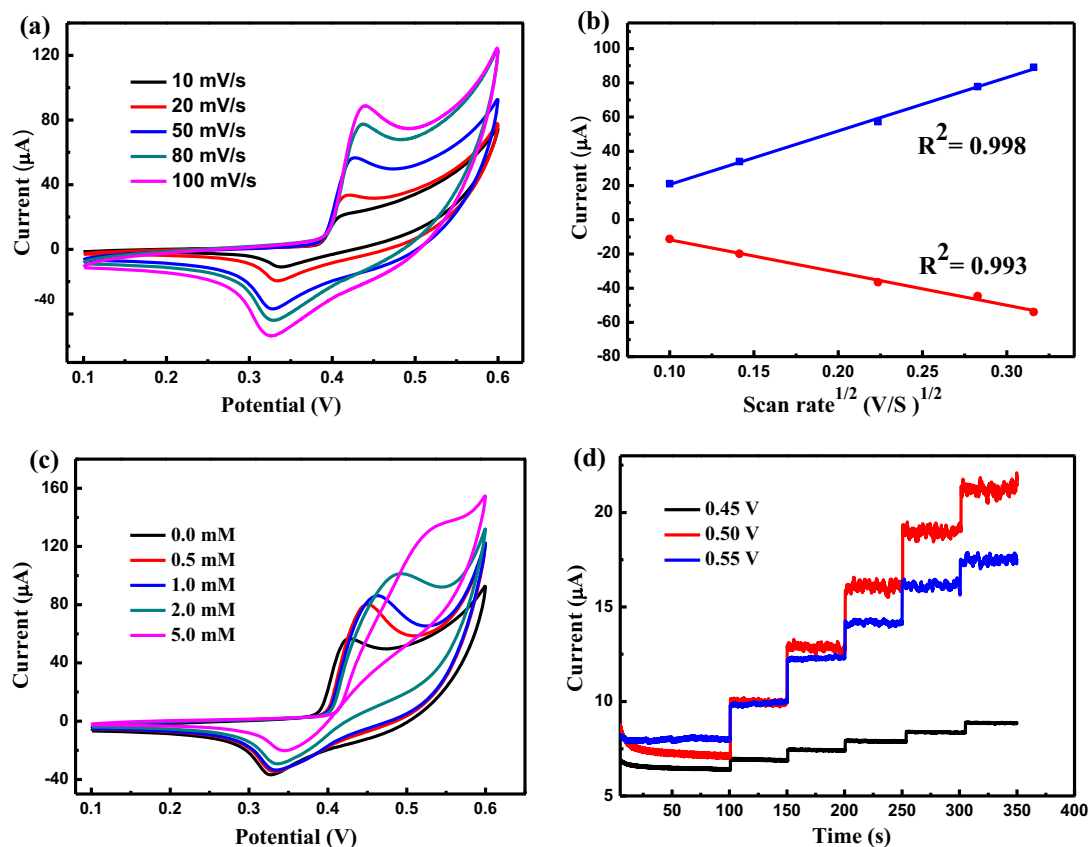
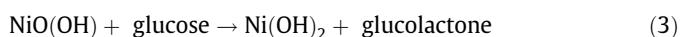
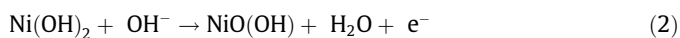


Fig. 5. (a) Cyclic voltammograms of RGO/Ni nanocomposites electrode at different scan rates in 0.1 M NaOH; (b) the variation of the peak current densities for RGO/Ni electrode as a function of the square root of scan rate; (c) cyclic voltammograms of RGO/Ni electrode in 0.1 M NaOH in the presence of various concentrations of glucose at scan rate of 50 mV/s; (d) amperometric responses of RGO/Ni nanocomposites electrode at different potentials in 0.1 M NaOH with successive addition of 100 μ M glucose.

the RGO/Ni electrode in the presence of various concentrations of glucose. As can be seen, when the concentration of glucose increases from 0 to 5.0 mM, the electrooxidation peak currents present a continuous increase and the oxidation potentials also shift to more positive values, suggesting better electrocatalytic activity of RGO/Ni nanocomposites toward glucose oxidation. The catalytic reaction was performed for the oxidation of glucose to glucolactone according to the following reactions [39,40]:



It is well known that the detection potential strongly affects the amperometric response of the electrode to glucose. Thus, chronoamperometry experiments were performed at various applied potentials for the RGO/Ni electrode by successive additions of 100 μ M glucose to 0.1 M NaOH solution at 50 s interval. As shown in Fig. 5d, a higher current response is observed at 0.5 V, which was then selected as the optimum working potential in the following experiments.

The amperometric response of the RGO/Ni electrode was further evaluated by successive injection of glucose into 0.1 M NaOH with the solution stirred constantly at 0.5 V. As can be seen in Fig. 6a, the RGO/Ni electrode shows a remarkable response to the changes of glucose concentration, which suggests the sensitive responses of RGO/Ni electrode to glucose oxidation reaction. The corresponding calibration curve based on the amperometric

results is shown in Fig. 6b. The amperometric response is linearly correlated with glucose concentration in the range of 0.01–3.0 mM with a correlation coefficient of 0.997. The sensitivity is 535.3 $\mu\text{A mM}^{-1} \text{cm}^{-2}$ and the detection limit can reach as low as 2.8 μM based on a signal-to-noise ratio of 3. In order to evaluate the performance of our prepared RGO/Ni electrode, a comparison of the RGO/Ni with other non-enzymatic glucose sensors is shown in Table 1. It is worth mentioning that the electrocatalytic performance in terms of the sensitivity, detection limit and linear range of RGO/Ni electrode for glucose detection are comparable with or even better than those obtained electrodes listed in the table.

In non-enzymatic glucose sensor applications, the elimination of interference responses toward species which having electroactivities similar to the target analyte is highly significant for the practical utilization of the electrodes. In this study, some easily oxidative species, such as ascorbic acid (AA), uric acid (UA) and dopamine (DA), which normally coexist with glucose in food and biological samples, were examined. The normal physiological level of glucose is about 30 times of interfering species, while the ratio is even higher in food samples [46]. The anti-interference effect of the as-prepared RGO/Ni electrode was tested by the addition of 0.1 mM of glucose at 0.5 V, followed by the additions of 0.02 mM of interfering species and 0.1 mM of glucose gradually to a 0.1 M NaOH solution, as shown in Fig. 7. It is clearly seen that an obvious glucose response was obtained, while negligible amperometric responses were observed for all the interfering species. This result demonstrates that the RGO/Ni electrode has a good specificity for glucose detection.

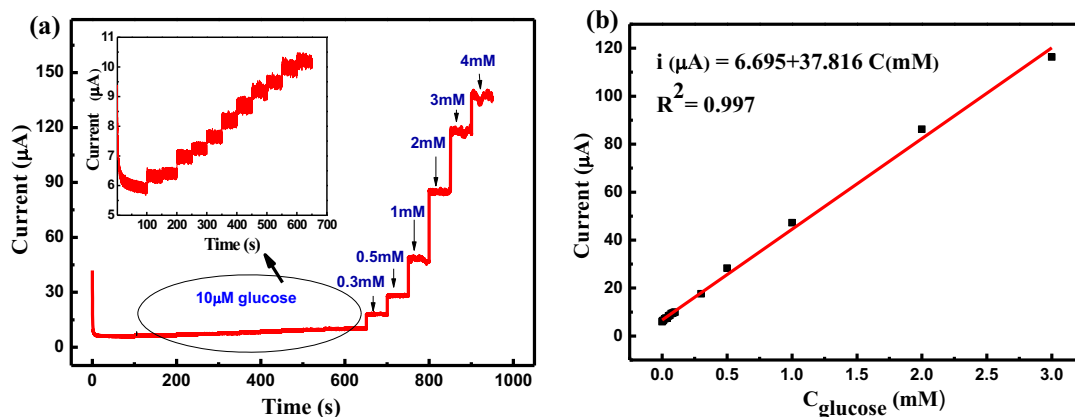


Fig. 6. (a) Amperometric response of RGO/Ni electrode to successive additions of glucose at an applied potential of 0.5 V. Inset is the enlarged amperometric current response of the areas marked by black ellipse; (b) the linear relationship between the response current and the glucose concentration.

Table 1

Comparison of the analytical performance of our proposed RGO/Ni electrode with other materials based non-enzymatic glucose sensors.

Glucose sensor	Linear range (mM)	Sensitivity ($\mu\text{A mM}^{-1} \text{cm}^{-2}$)	Detection limit (μM)	Ref.
RGO-Ni(OH) ₂	0.002–3.1	11.43	0.6	37
PVP-GNs-Ni-CS	0.0001–0.5	103.8	0.03	40
NiO/graphene	0.02–2.0	225.619	5.0	41
Ni/POAP/CPE	0.1–2.7	38.07	90	42
Ti/TiO ₂ /Ni	0.1–1.7	200	4	43
GOD-Ag@C	0.05–2.5	24.65	20	44
RGO/Ag/GOD	0.5–12.5	3.84	160	45
RGO/Ni	0.01–3.0	535.3	2.8	This work

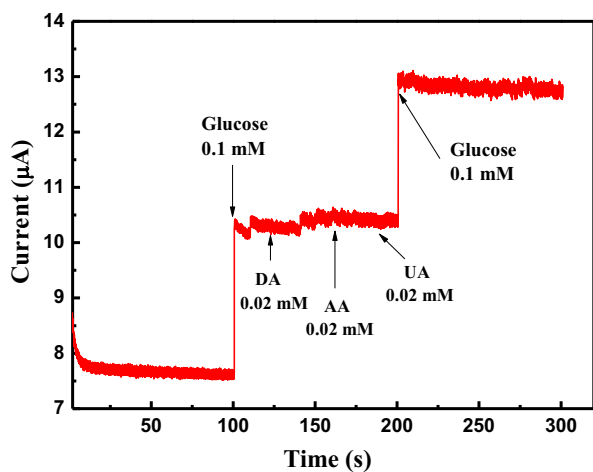


Fig. 7. Amperometric response of the RGO/Ni electrode at 0.5 V with successive additions of different analytes.

4. Conclusions

In summary, a facile refluxing approach has been developed to synthesize the RGO supported Ni nanoparticles. By using triethylene glycol as both reductive and dispersing agent, highly dispersed Ni nanoparticles with interesting hexagonal close-packed structure were homogeneously deposited on the surface of RGO sheets. Enhanced catalytic activity comparable to noble metal catalysts toward the reduction of *p*-nitrophenol by NaBH₄ was obtained. When used as electrode material for glucose detection, the RGO/Ni also shows prominent electrocatalytic activity with lower detection limit, higher sensitivity, wider linear range and excellent selectivity in contrast with previously published

electrode materials. This facile one-step route can be extended to synthesize other metal nanostructures on RGO nanosheets with various morphologies and functions, and provides a new approach to advanced catalysts.

Acknowledgements

The authors are grateful for financial support from the National Natural Science Foundation of China (Nos. 51272094 and 51602129), the Natural Science Foundation of Jiangsu Province (No. BK20150507), China Postdoctoral Science Foundation (Nos. 2015M580392 and 2015M580393), Jiangsu Planned Projects for Postdoctoral Research Funds (Nos. 1501025B and 1601231C) and the Startup Fund for Distinguished Scholars of Jiangsu University (No. 15JDG023).

Appendix A. Supplementary material

Supplementary data associated with this article can be found, in the online version, at <http://dx.doi.org/10.1016/j.jcis.2016.10.045>.

References

- [1] J. Gu, Y.W. Zhang, F. Tao, *Chem. Soc. Rev.* 41 (2012) 8050–8065.
- [2] E. Gross, G.A. Somorjai, *J. Catal.* 328 (2015) 91–101.
- [3] M.G. Castano, T.R. Reina, S. Ivanova, M.A. Centeno, J.A. Odriozola, *J. Catal.* 314 (2014) 1–9.
- [4] A.P. LaGrow, B. Ingham, S. Cheong, G.V.M. Williams, C. Dotzler, M.F. Toney, D.A. Jefferson, E.C. Corbos, P.T. Bishop, J. Cookson, R.D. Tilley, *J. Am. Chem. Soc.* 134 (2011) 855–858.
- [5] X. Li, A. Dhanabalan, C. Wang, *J. Power Sources* 196 (2011) 9625–9630.
- [6] I.M. Sadiq, A.M. Mohammad, M.E. El-Shakre, M.S. El-Deab, *Int. J. Hydrogen Energy* 37 (2012) 68–77.
- [7] Z. Chen, J. Guo, T. Zhou, Y. Zhang, L. Chen, *Electrochim. Acta* 109 (2013) 532–535.
- [8] N. Hadian, M. Rezaei, *Fuel* 113 (2013) 571–579.

- [9] S. Pisiewicz, D. Formenti, A.E. Surkus, M. Martina Pohl, J. Radnik, K. Junge, C. Topf, S. Bachmann, M. Scalone, M. Beller, *ChemCatChem* 8 (2016) 129–134.
- [10] X. Huang, X.Y. Qi, F. Boey, H. Zhang, *Chem. Soc. Rev.* 41 (2012) 666–686.
- [11] S. Bai, X.P. Shen, *RSC Adv.* 2 (2012) 64–98.
- [12] T. Xiong, F. Dong, Y. Zhou, M. Fu, W.K. Ho, *J. Colloid Interf. Sci.* 447 (2015) 16–24.
- [13] C.C. Huang, C. Li, G.Q. Shi, *Energy Environ. Sci.* 5 (2012) 8848–8868.
- [14] B.F. Machado, Philippe Serp, *Catal. Sci. Technol.* 2 (2012) 54–75.
- [15] H.G. Yu, J. Tian, F. Chen, P. Wang, X.F. Wang, *Sci. Rep.* 5 (2015) 13083.
- [16] Q. Li, X. Li, S. Wageh, A.A. Al-Ghamdi, J.G. Yu, *Adv. Energy Mater.* 5 (2015) 1500010.
- [17] T.T. Chen, F. Deng, J. Zhu, C.F. Chen, G.B. Sun, S.L. Ma, X.J. Yang, *J. Mater. Chem.* 22 (2012) 15190–15197.
- [18] Z.Y. Ji, X.P. Shen, G.X. Zhu, H. Zhou, A.H. Yuan, *J. Mater. Chem.* 22 (2012) 3471–3477.
- [19] W.S. Hummers, R.E. Offeman, *J. Am. Chem. Soc.* 80 (1958) 1339.
- [20] Z.Y. Ji, X.P. Shen, J.L. Yang, G.X. Zhu, K.M. Chen, *Appl. Catal. B* 144 (2014) 454–461.
- [21] T. Nakajima, A. Mabuchi, R. Hagiwara, *Carbon* 26 (1988) 357–361.
- [22] D. Graf, F. Molitor, K. Ensslin, C. Stampfer, A. Jungen, C. Hierold, L. Wirtz, *Nano Lett.* 7 (2007) 238–242.
- [23] B.B. Zhang, J.L. Song, G.Y. Yang, B.X. Han, *Chem. Sci.* 5 (2014) 4656–4660.
- [24] A.C. Ferrari, J.C. Meyer, V. Scardaci, C. Casiraghi, M. Lazzeri, F. Mauri, S. Piscanec, D. Jiang, K.S. Novoselov, S. Roth, A.K. Geim, *Phys. Rev. Lett.* 97 (2006) 13831–13840.
- [25] M.S. Dresselhaus, A. Jorio, M. Hofmann, G. Dresselhaus, R. Saito, *Nano Lett.* 10 (2010) 751–758.
- [26] G. Liu, Y.J. Wang, F.Y. Qiu, L. Li, L.F. Jiao, H.T. Yuan, *J. Mater. Chem.* 22 (2012) 22542–22549.
- [27] J. Gao, F. Liu, Y.L. Liu, N. Ma, Z.Q. Wang, X. Zhang, *Chem. Mater.* 22 (2010) 2213–2218.
- [28] H.H. Zhang, Q. Liu, K. Feng, B. Chen, C.H. Tung, L.Z. Wu, *Langmuir* 28 (2012) 8224–8229.
- [29] J. Kim, L.J. Cote, F. Kim, W. Yuan, K.R. Shull, J. Huang, *J. Am. Chem. Soc.* 132 (2010) 8180–8186.
- [30] H. Bai, C. Li, G.Q. Shi, *Adv. Mater.* 23 (2011) 1089–1115.
- [31] K.L. Wu, X.W. Wei, X.M. Zhou, D.H. Wu, X.W. Liu, Y. Ye, Q. Wang, *J. Phys. Chem. C* 115 (2011) 16268–16274.
- [32] B. Baruah, G.J. Gabriel, M.J. Akbashev, M.E. Boohar, *Langmuir* 29 (2013) 4225–4234.
- [33] Y.W. Zhang, S. Liu, W.B. Lu, L. Wang, J.Q. Tian, X.P. Sun, *Catal. Sci. Technol.* 1 (2011) 1142–1144.
- [34] J. Li, C.Y. Liu, Y. Liu, *J. Mater. Chem.* 22 (2012) 8426–8430.
- [35] K.E. Toghill, R.G. Compton, *Int. J. Electrochem. Sci.* 5 (2010) 1246–1301.
- [36] Z.G. Wang, Y. Hu, W.L. Yang, M.J. Zhou, X. Hu, *Sensors* 12 (2012) 4860–4869.
- [37] Y. Zhang, F.G. Xu, Y.J. Sun, Y. Shi, Z.W. Wen, Z. Li, *J. Mater. Chem.* 21 (2011) 16949–16954.
- [38] S.Q. Ci, Z.H. Wen, S. Mao, Y. Hou, S.M. Cui, Z. He, J.H. Chen, *Chem. Commun.* 51 (2015) 9354–9357.
- [39] J. Song, L. Xu, R.Q. Xing, W.F. Qin, Q.L. Dai, H.W. Song, *Sens. Actuators, B* 182 (2013) 675–681.
- [40] Z.G. Liu, Y.J. Guo, C. Dong, *Talanta* 137 (2015) 87–93.
- [41] X.H. Zhu, Q.F. Jiao, C.Y. Zhang, X.X. Zuo, X. Xiao, Y. Liang, J.M. Nan, *Microchim. Acta* 180 (2013) 477–483.
- [42] R. Ojani, J.B. Raoof, S. Fathi, *Electroanalysis* 20 (2008) 1825–1830.
- [43] C. Li, Y. Su, S. Zhang, X. Lv, H. Xia, Y. Wang, *Biosens. Bioelectron.* 26 (2010) 903–907.
- [44] X. Zhou, X.X. Dai, J.G. Li, Y.M. Long, W.F. Li, Y.F. Tu, *Mater. Sci. Eng. C* 49 (2015) 579–587.
- [45] S. Palanisamy, C. Karupiah, S.M. Chen, *Colloids Surf. B: Biointerf.* 114 (2014) 164–169.
- [46] J. Luo, S.S. Jiang, H.Y. Zhang, J.Q. Jiang, X.Y. Liu, *Anal. Chim. Acta* 709 (2012) 47–53.